AGU ADVANCING EARTH AND SPACE SCIENCES

Geophysical Research Letters®

Key Points:

- Oblique chorus subpackets are generated in the 2-D GCPIC simulation model
- Electron hole associated with the inhomogeneity factor oscillates with time during subpacket formation
- Cyclotron and Landau resonances coexist during subpacket formation

Correspondence to:

X. Wang and H. Chen,
wangxue@auburn.edu;
huayue_chen@foxmail.com

Resonant Electron Signatures in the Formation of Chorus Wave Subpackets

Xueyi Wang[1] , Huayue Chen[1] , Yoshiharu Omura[2] , Yi-Kai Hsieh[2] , Lunjin Chen[3] , Yu Lin[1] , Xiao-Jia Zhang[3] , and Zhiyang Xia[3]

[1]Department of Physics, Auburn University, Auburn, AL, USA, [2]Research Institute for Sustainable Humanosphere, Kyoto University, Kyoto, Japan, [3]William B. Hanson Center for Space Sciences, University of Texas at Dallas, Richardson, TX, USA

Abstract A 2-D GCPIC simulation in a dipole field system has been conducted to explore the excitation of oblique whistler mode chorus waves driven by energetic electrons with temperature anisotropy. The rising tone chorus waves are initially generated near the magnetic equator, consisting of a series of subpackets, and become oblique during their propagation. It is found that electron holes in the wave phase space, which are formed due to the nonlinear cyclotron resonance, oscillate in size with time during subpacket formation. The associated inhomogeneity factor varies accordingly, giving rise to various frequency chirping in different phases of subpackets. Distinct nongyrotropic electron distributions are detected in both wave gyrophase and stationary gyrophase. Landau resonance is found to coexist with cyclotron resonance. This study provides multidimensional electron distributions involved in subpacket formation, enabling us to comprehensively understand the nonlinear physics in chorus wave evolution.

Plain Language Summary Subpackets are a series of wave packets within chorus waves, characterized by wave amplitude modulation. In this study, we investigate the electron distributions in various phase spaces associated with subpacket formation, by performing a two-dimensional simulation in a dipole field. It is found that the electrons can be trapped in the wave phase space through both cyclotron and Landau resonances. These two resonance interactions can also produce the "bump" and "plateau" shapes in momentum space, as well as the fine density structures in spatial space. Therefore, both cyclotron and Landau resonances play an important role in subpacket formation. Our study provides new inspiration for the nonlinear theory of chorus subpackets.

1. Introduction

Chorus waves are intense whistler-mode emissions, commonly observed in the Earth's (Burtis & Helliwell, 1969; Horne & Thorne, 1998; Tsurutani & Smith, 1974) and other planets' magnetospheres (Coroniti et al., 1980; Harada et al., 2016; Hospodarsky et al., 2008). They play a crucial role in electron dynamics, including the acceleration of hundreds of keV electrons (Meredith et al., 2001; Omura et al., 2019; Thorne et al., 2013), and the precipitation of tens of keV electrons (L. Chen et al., 2020; Ozaki et al., 2018) due to pitch angle scattering/diffusion (Liu et al., 2015; Xiao et al., 2009, 2010). The spectrum of chorus waves typically contains discrete rising tone elements, and each element consists of a series of subpackets, with wave amplitude modulation at intervals of ~10–100 milliseconds (R. Chen, Tsurutani, et al., 2022; H. Chen, Wang, et al., 2023; Crabtree, Gurudas Ganguli, & Tejero, 2017; Santolík et al., 2003, 2014; Tsurutani et al., 2020; Zhang et al., 2020). The subpackets have been suggested to play an important role in producing the fine structures in microbursts (Miyoshi et al., 2015; Ozaki et al., 2018) and electron acceleration (Foster et al., 2021; Kubota & Omura, 2018).

The superposition theory has been proposed to explain the subpacket formation, with a requirement of an artificial frequency difference in simultaneous presence of two chorus waves (Nunn et al., 2021; Zhang et al., 2020). Tao et al. (2017) speculated subpacket formation as a part of nonlinear processes, in which the energy of phase-trapped electrons oscillates in the trapping period, and thus the wave amplitude is modulated. The authors suggested that the process is similar to the nonlinear Landau resonance, expecting the energy conservation between waves and particles (O'Neil, 1965). Crabtree, Ganguli, and Tejero (2017) suggested that the multiple clumps of electrons in phase space can also cause subpacket formation, and are generated due to a higher order resonance in wave-particle interactions. Another model based on sequential triggering model (Omura & Nunn, 2011) has also been developed, by assuming that a new emission is generated by resonant currents released from the upstream

region, where the resonant currents are formed due to the nonlinear interactions with previous trigger waves (Hanzelka et al., 2020). These models are derived only for parallel chorus subpackets, whereas the formation of subpackets for more realistic oblique chorus waves is less understood. Chorus wave obliquity is a natural property of wave propagation in the inhomogeneous dipole field (L. Chen et al., 2013), and subpacket structures of oblique waves are principally important for modeling the efficiency of wave-particle interactions.

In this study, we have performed a two-dimensional (2-D) particle-in-cell (PIC) simulation to produce the oblique chorus waves, and provide multidimensional electron information during subpacket formation. These signals reveal the electron dynamics associated with nonlinear wave-particle interactions, which helps us to comprehensively understand the physical processes involved in subpacket formation.

2. Simulation Model and Initial Setup

The simulation has been conducted in the meridian plane by using the general curvilinear plasma simulation code (GCPIC) model (Lu et al., 2019). In this model, the cold electrons satisfy a Maxwellian distribution, while the energetic electrons follow a bi-Maxwellian distribution. Both cold electrons and energetic electrons are treated as particles and are pushed by the relativistic Lorentz force. Ions are immobile. The reflecting boundary condition is employed for particles, and the absorbing boundary condition is used for waves. In this study, the GCPIC model has been implemented by using three-dimensional (3-D) particle trajectories, in which the particles are advanced following their 3-D velocities and positions in the curvilinear coordinates (p,q,w), where $\hat{p}$ is along the L direction, $\hat{q}$ is antiparallel to the background magnetic field, and $\hat{w}$ is the azimuthal direction.

At the magnetic equator, the number density of cold electrons n_{e0} is assumed $\propto L^{-4}$ (Denton et al., 2004). The ratio between the electron plasma frequency and the electron gyrofrequency in the center of simulation domain (L_0) is $\omega_{pe}/\Omega_{e0} = 4.98$, where $\omega_{pe} = \sqrt{n_{e0}e^2/m_e\varepsilon_0}$ and $\Omega_{e0} = eB_{e0}/m_e$, B_{e0} is the equatorial background magnetic field, ε_0 is the vacuum permittivity, and e and m_e are the charge and mass of an electron. The number density, parallel thermal momentum, and the temperature anisotropy of energetic electrons at the magnetic equator are $n_{heq}/n_{e0} = 0.008$, $U_{\|}/V_{Ae0} = 0.984$ ($V_{Ae0} = B_{e0}/\sqrt{\mu_0 n_{e0}m_e}$ is the equatorial electron Alfven speed with μ_0 being the vacuum permeability), and $U_{\perp t}^2/U_{\|t}^2 = 6$, where "$\|$" and "$\perp$" represent the directions parallel and perpendicular to the background magnetic field B_0 here and after. A reduced dipole field system centered at $p_0 = 1639 V_{Ae0}/\Omega_{e0}$, corresponding to $L_0 = 0.6$, is used. The simulation domain consists of $400 \times 9{,}984$ grids in the p-q plane and cover a latitude range of $-31° < \lambda < 31°$, with the average grid length of $\Delta p = 0.64 V_{Ae0}/\Omega_{e0}$ and $\Delta q = 0.16 V_{Ae0}/\Omega_{e0}$. The total particle number is 8×10^9. The time step is $\Omega_{e0}\Delta t = 0.02$.

3. Simulation Results

Chorus waves are excited by energetic electrons. The wave amplitudes in the southern hemisphere are shown in Movie S1. It is seen that the waves propagate nearly opposite to field lines. Figure 1a shows the variation of $\delta B_{\perp 1}$ ("⊥1" denoting the $\hat{p}$ direction) in the h-t plane at $p = 1722 V_{Ae0}/\Omega_{e0}$, with h denoting the distance along field line to the magnetic equator. The negative (positive) values of h correspond to the positions in the southern (northern) hemisphere. A series of wave subpackets with spatiotemporally modulated amplitudes, as shown as Subp#1-#3, constitute a chorus element. Figures 1b–1g present the wave properties at $h = -242.42 V_{Ae0}/\Omega_{e0}$ (corresponding to a magnetic latitude of $\lambda = -7.57°$), displaying (b) disturbed magnetic fields: $\delta B_{\|}$, $\delta B_{\perp 1}$, and $\delta B_{\perp 2}$ ("⊥2" denoting the $\hat{w}$ direction), (c) spectrum of δB^2, (d) wave normal angle θ, (e) θ_s, the angle between wave Poynting flux and background magnetic field, (f) wave amplitude δB, and (g) instantaneous wave frequency ω. The instantaneous wave frequency ω is determined as the inverse of the interval between the start and end times of the half-wave cycles, which are estimated from the zero-crossings of $\delta B_{\perp 1}$. As shown in Figure 1b, the compressional component of magnetic field is quite smaller than the transverse components with $|\delta B_{\|}|/\delta B < {\sim}30\%$. Three subpackets are found in $\Omega_{e0}t = 2{,}770$–$3{,}250$. The spectrum in Figure 1c exhibits a rising tone structure from ${\sim}0.25\Omega_{e0}$ to ${\sim}0.60\Omega_{e0}$, with a weak power gap at $\omega \sim 0.5\Omega_{e0}$. In Figure 1d, the wave normal angle is close to $0°$ at smaller frequency $\omega \sim 0.25\Omega_{e0}$, while it gets larger at $\omega \geq 0.3\Omega_{e0}$. The wave normal angle reaches its maximum of ${\sim}30°$ at $\omega \sim 0.6\Omega_{e0}$ in the upper band. However, the angle between wave Poynting flux and background magnetic field is still quite small (with $180° - \theta_s < 10°$). Based on the temporal evolution of wave amplitude (Figure 1f), the growth rate for subpackets is ${\sim}10^{-2}\Omega_{e0}$, greatly larger than that estimated from linear calculation (${\sim}10^{-3}\Omega_{e0}$). The instantaneous wave frequency in Figure 1g exhibits an overall trend of upward chirping, however, it displays
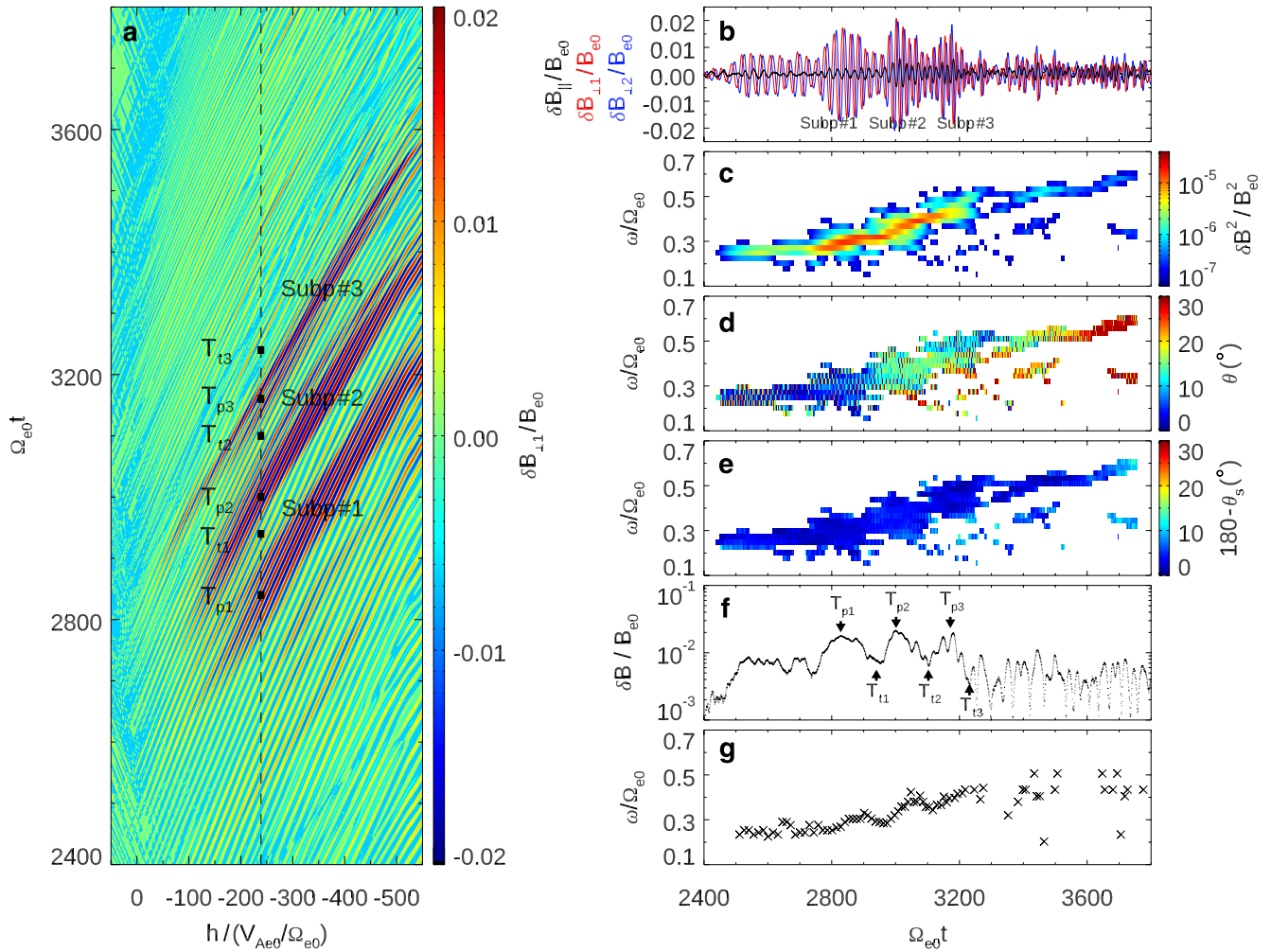
Figure 1. (a) The disturbed magnetic field $\delta B_{\perp 1}$ in the h-t plane, where h represents the distance along the field line at $p = 1722 V_{Ae0}/\Omega_{e0}$ from the magnetic equator. The position of $h = -242.24 V_{Ae0}/\Omega_{e0}$ is marked by a dashed line, corresponding to a magnetic latitude of $\lambda = -7.57^{\circ}$. (b) Three disturbed magnetic components: $\delta B_{\parallel}$ (black), $\delta B_{\perp 1}$ (red), and $\delta B_{\perp 2}$ (blue), (c) spectrum of δB^2, (d) wave normal angle θ, (e) $180^{\circ} - \theta_s$, (f) wave amplitude δB, and (g) instantaneous wave frequency ω. In panels (a, b), three subpackets are denoted by "Subp#1-#3." Six time points ($\Omega_{e0}T_{p1} = 2,840$, $\Omega_{e0}T_{t1} = 2,940$, $\Omega_{e0}T_{p2} = 3,000$, $\Omega_{e0}T_{t2} = 3,100$, $\Omega_{e0}T_{p3} = 3,160$, and $\Omega_{e0}T_{t3} = 3,230$) are marked by the arrows in panel (f). At each time point, the energetic electrons are collected in a spatial scale smaller than one wavelength and in a time scale shorter than one wave period, as illustrated by the small box in panel (a).

slightly downward chirping signals between adjacent subpackets, where the wave amplitudes meet the local minima.

We select six time points (marked by the arrows in Figure 1f) to demonstrate the electron distributions during subpacket formation. The time points T_{p1}, T_{p2}, and T_{p3} (T_{t1}, T_{t2}, and T_{t3}) corresponds to subpacket peaks (subpacket troughs), at which the wave amplitude reaches its maximum (minimum).

Figure 2 shows the disturbed distribution $\delta f = f - f_0$ of energetic electrons in the phase space (ζ, $v_{\parallel}$) at $\Omega_{e0}T_{p2} = 3,000$ for the $v_{\perp}$ channels of $v_{\perp}/V_{Ae0} = $ (a) 1–2, (b) 2–3, (c) 3–4, and (d) 4–5. Here ζ is the wave gyrophase angle between $v_{\perp}$ and $\delta B_{\perp}$ (Figure S1 in Supporting Information S1), and f_0 is the initial distribution. The wave frequency and wave normal angle at T_{p2} are $\omega/\Omega_{e0} = 0.3259$ and $\theta = 16.44^{\circ}$, where the wave number is estimated as $kV_{Ae0}/\Omega_{e0} = -0.7174$ from the cold plasma dispersion relation, with the negative sign denoting the propagation against field line ($\boldsymbol{k} \cdot \boldsymbol{B}_0 < 0$). The cyclotron resonance velocity is calculated as $v_c = (\omega - \Omega_e/\gamma)/k_{\parallel}$, where $\Omega_e = eB_0/m_e$ is the local electron gyrofrequency, $\gamma = \left[1 - \left(v_{\parallel}^2 + v_{\perp}^2\right)/c^2\right]^{-1/2}$ is the Lorentz factor, and c is the light speed. The v_c is calculated as $v_c/V_{Ae0} = 0.8876$ (0.7634, 0.5476, and 0.1474) by using $v_{\perp}/V_{Ae0} = 1.5$ (2.5, 3.5, and 4.5). Around v_c, electron hole is formed in $\zeta \approx -\pi - \pi/2$, exhibiting negative δf. As $v_{\perp}$ increases, the
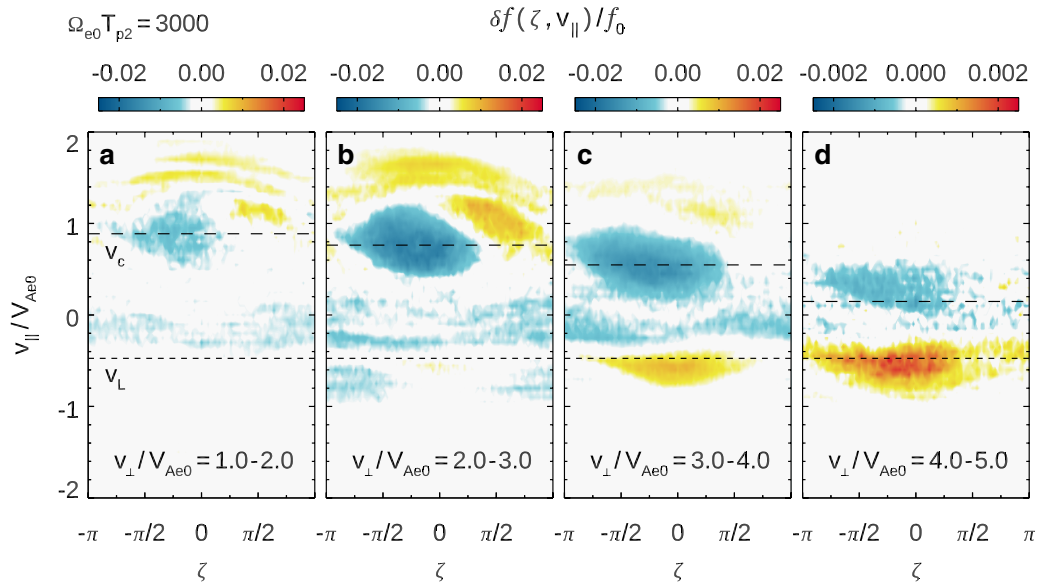
Figure 2. The disturbed distribution $\delta f(\zeta, v_\parallel)/f_0$ at $\Omega_{e0}T_{p2} = 3{,}000$ for the $v_\perp$ channels of $v_\perp/V_{Ae0} =$ (a) 1.0–2.0, (b) 2.0–3.0, (c) 3.0–4.0, and (d) 4.0–5.0. In each panel, the dashed and dotted line represent cyclotron resonance velocity v_c and Landau resonance velocity v_L, respectively.

electron hole shifts toward smaller $v_\parallel$, consistent with the decrease of v_c. Among the four $v_\perp$ channels, the electron hole for $v_\perp/V_{Ae0} = 2$–3 is the deepest. Electron hill with positive δf at relatively larger $v_\parallel$ is found to accompany with electron hole due to particle number conservation. In addition, electrons are also trapped in the phase space around the Landau resonance velocity v_L with positive δf, where $v_L = \omega/k_\parallel = -0.4736 V_{Ae0}$. The Landau resonance dominates at larger $v_\perp$ (Figures 2c and 2d), implying that it is controlled by the effective parallel electric field $\delta E_\parallel^* = (v_\perp \times \delta B_\perp)/c$, in addition to the electrostatic component of electric field $\delta E_\parallel$. Therefore, electrons can be trapped in the wave phase of oblique chorus waves through both cyclotron and Landau resonances. The distributions at another time point $\Omega_{e0}T_{p1} = 2{,}840$ is presented in Figure S2 in Supporting Information S1 for reference.

Figure 3 shows the $\delta f(\zeta, v_\parallel)$ of energetic electrons for $v_\perp/V_{Ae0} = 2$–3 at all six time points. It is found that the central position of electron hole in $v_\parallel$ is around v_c, where v_c decreases with time due to the upward frequency chirping (Figure 1c). Meanwhile, the central position in ζ temporally oscillates with the period of $\sim 160\Omega_{e0}^{-1}$, corresponding to the period of subpackets. The electron hole locates in $\zeta \approx -\pi - \pi/2$ at subpacket peaks (Figures 3a, 3c, and 3e), while it gets wider to $\zeta \approx -\pi - \pi$ at subpacket troughs (Figures 3b, 3d, and 3f). The electron hole at subpacket troughs is more flattered, and the area within the hole is found to be nearly constant during oscillation. The magenta curve represents the envelope of the electron hole, which is estimated from Omura et al. (2008):

$$k^2\left(v_\parallel - v_c\right)^2 + 2\omega_{tr}^2\left[\cos(\zeta + \pi) - S(\zeta + \pi)\right] = C, \tag{1}$$

where $\omega_{tr} = \omega_t\chi\gamma^{-1/2}$ with the trapping frequency $\omega_t = (kv_\perp e\delta B/m_e)^{1/2}$ and $\chi = \left[1 - \omega^2/(k^2c^2)\right]^{1/2}$, S is the inhomogeneity factor, and C is a constant. The $v_\perp$ is set to be $2.5V_{Ae0}$. The wave parameters (ω, k, δB, and v_c) are listed in Table S1 in Supporting Information S1. The S values at six time points are estimated through Equation 1 as -0.35, -0.01, -0.34, -0.02, -0.38, and -0.05, respectively. Note that at subpacket peaks, S is ~ -0.4, indicating the maximum energy transfer between waves and particles. While at subpacket troughs, S is ~ 0.

The theoretical inhomogeneity factor S_{th} can be calculated from Hsieh and Omura (2023):

$$S_{th} = \frac{1}{\Omega_{t,1}^2}\left\{-\left(\frac{v_r}{v_{g\parallel}} - 1\right)^2\frac{\partial\omega}{\partial t} + \left[\frac{v_r}{\gamma} - \frac{k_\parallel v_\perp^2}{2\Omega_e} - \frac{v_r^2\omega_{pe}}{2c}\left(\frac{\Omega_e}{\omega}\cos\theta - 1\right)^{-\frac{3}{2}}\frac{\cos^2\theta}{\omega}\right]\frac{\partial\Omega_e}{\partial h}\right\}, \tag{2}$$
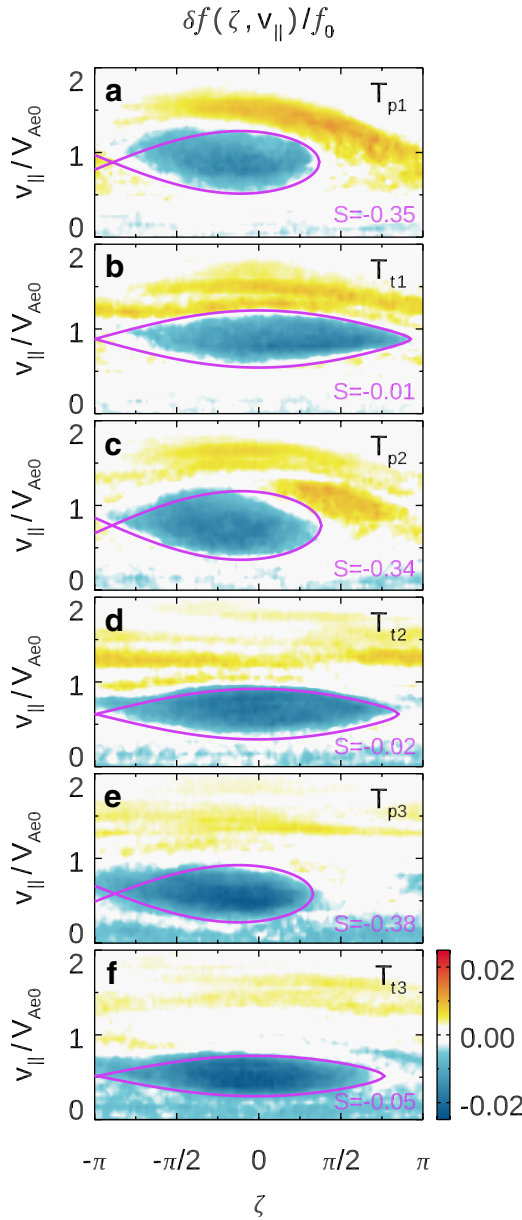
where

$$\delta f(\zeta, v_{\parallel})/f_0$$

Figure 3. The disturbed distribution $\delta f(\zeta, v_{\parallel})/f_0$ at six time points (from top to bottom: T_{p1}, T_{t1}, T_{p2}, T_{t2}, T_{p3}, T_{t3}). In each panel, the magenta curve represents the envelope of electron hole, and the corresponding S value is displayed in magenta.

$$\Omega_{t,1}^2 = \frac{1}{\gamma}\left(\omega_{t,1}^2 - \omega\Omega_{d,1}\right), \qquad (3)$$

$$\omega_{t,1}^2 = \frac{ek_{\parallel}}{m_e}\left[\delta E_{\parallel}\boldsymbol{J}_1(\beta) + v_{\perp}\delta B\boldsymbol{J}_0(\beta)\right], \qquad (4)$$

and

$$\Omega_{d,1} = \frac{e}{m_e c^2}\left[v_{\parallel}\delta E_{\parallel}\boldsymbol{J}_1(\beta) + v_{\perp}\delta E\boldsymbol{J}_0(\beta)\right]. \qquad (5)$$

Here $v_{g\parallel}$ is the parallel component of the group velocity, $k_{\parallel}$ and $k_{\perp}$ are the parallel and perpendicular wave numbers, δE is the electric field amplitude, and $\delta E_{\parallel}$ is the parallel component. Additionally, $\boldsymbol{J}_n(\beta)$ is the n-order (with n being the nonnegative integer) Bessel function of the first kind, with $\beta = k_{\perp}\rho$ and $\rho = v_{\perp}/\Omega_{e0}$ being the electron gyroradius. By given the chirping rate and the gradient of background magnetic field obtained from the simulation (Table S1 in Supporting Information S1), we evaluate S_{th} under different stages of subpackets: $S_{th} = -0.34$, 0.01, -0.31, 0.03, -0.33, and -0.08, respectively. The value of S_{th} is well consistent with the S estimated from electron hole in simulation. Note that at subpackets peaks, both frequency chirping term ($\partial\omega/\partial t \sim 10^{-3}$) and field gradient term ($\partial B_0/\partial h = 5.6 \times 10^{-4} B_{e0}/\left(V_{Ae0}\Omega_{e0}^{-1}\right)$) contribute to negative inhomogeneities, where the frequency chirping term is dominated, leading to $S_{th} \sim -0.4$. While at amplitude troughs, the two terms are comparable but have opposite signs due to the weak downward chirping ($\partial\omega/\partial t \sim -10^{-4}$), resulting in $S_{th} \sim 0$.

Figure 4 shows the momentum ($u = \gamma v$) distributions of energetic electrons at T_{p2} and T_{t2}. As shown in Figures 4a and 4b, the electron distribution $f(u_{\parallel}, u_{\perp})$ exhibits significantly variations around $u_c = (\Omega_e - \gamma\omega)/k_{\parallel}$ and $u_L = \gamma\omega/k_{\parallel}$, indicating strong wave-particle interactions through both cyclotron and Landau resonances. The $f(u_{\parallel}, u_{\perp})$ decreases obviously at u_c and $u_{\perp}/V_{Ae0} > 2$, corresponding to the density reduction at electron hole in the wave phase (Figures 3c and 3d). To specify the distribution in the parallel direction, we plot f as a function of $u_{\parallel}$ in Figures 4c and 4d, where u_c and u_L are calculated using $u_{\perp}/V_{Ae0} = 2.5$, and the gray line represents the initial parallel distribution. At subpacket peak T_{p2}, a "plateau" shape is around cyclotron resonance velocity, while a "bump" shape is around Landau resonance velocity. An electron "beam" is assumed in the "bump" and contributes to the excitation of electron acoustic waves, which cause the time domain structures (An et al., 2019) in $\delta E_{\parallel}$ observed in our simulation. At subpacket trough T_{t2}, on the other hand, a "bump" exists around cyclotron resonance velocity while a "plateau" appears around Landau resonance velocity. The "bump" shape corresponds to the positive derivation of the distribution $\partial f/\partial |u_{\parallel}| > 0$, indicating a free energy resulting in chorus wave excitation via nonlinear/linear growth (Zonca et al., 2022). The "plateau" shape could contribute to wave damping (Chen, Chen, et al., 2023; H. Chen, Gao, et al., 2022). The alternating shapes at u_c and u_L during subpacket formation indicate the coexistence of cyclotron and Landau resonances in oblique chorus waves. The distributions at T_{p1} is also presented (Figure S3 in Supporting Information S1) for reference.

The electron distributions in the gyrophases are also depicted in Figure 4, showing the δf in the (e, f) wave gyrphase ($u_{\delta B_{\perp}}$, $u_{\delta E_{\perp}}$) and (g, h) stationary gyrophase ($u_{\perp 1}$, $u_{\perp 2}$). Note that the distributions have been averaged over one gyroperiod. It is seen that the nongyrotropic distributions present in both wave gyrophase and stationary gyrophase. In the wave gyrophase, the negative δf mainly locates in $\zeta \approx -\pi - \pi/2$ at subpacket peak in Figure 4e, corresponding to the inhomogeneity factor $S \sim -0.4$ as shown in Figures 3a, 3c, and 3e. While at subpacket trough
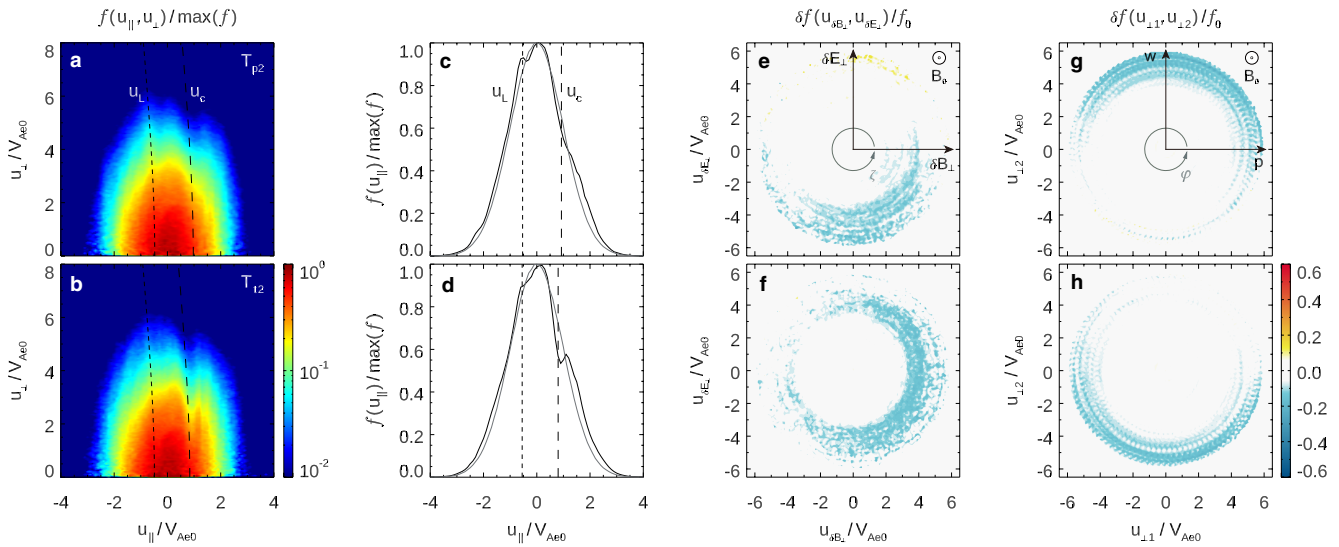
Figure 4. The normalized (a, b) momentum distribution $f(u_\parallel, u_\perp)$ and (c, d) parallel momentum distribution $f(u_\parallel)$, and the disturbed distributions δf in the (e, f) wave gyrophase ($u_{\delta B_\perp}$, $u_{\delta E_\perp}$) and (g, h) stationary gyrophase ($u_{\perp 1}$, $u_{\perp 2}$). The f is normalized to its maximum value. In panels (a–d), the dashed curve or line denotes u_c, and the dotted curve or line represents u_L. In panels (c, d), the gray line is the initial parallel distribution. The perpendicular momentums in the wave gyrophase $u_{\delta B_\perp}$ and $u_{\delta E_\perp}$ (stationary gyrophase $u_{\perp 1}$ and $u_{\perp 2}$) are defined along $\delta B_\perp$ and $\delta E_\perp$ ($\hat{p}$ and $\hat{w}$), respectively. The angle $\zeta(\varphi)$ represents the wave gyrophase (stationary gyrophase) angle. The top row corresponds to $\Omega_{e0} T_{p2} = 3,000$ and the bottom row corresponds to $\Omega_{e0} T_{t2} = 3,100$.

in Figure 4f, the distribution rotates to $\zeta \approx -\pi - \pi$. The negative δf is found to be bouncing with time in the wave gyrophase, corresponding to the oscillation of electron hole in the phase space (ζ, $v_\parallel$). Meanwhile, the non-gyrotropic distribution is also apparent in the stationary coordinates, characterized by electron bunching at large $v_\perp/V_{Ae0} \approx 4$–$6$. Such a pattern of electron bunching in the gyrophase has not been detected in a separated one-dimensional (1-D) simulation, in which chorus waves are limited to parallel propagation. The nongyrotropic distribution in the stationary gyrophase could be associated with the electron kinetic effects in the perpendicular direction due to $k_\perp \rho \geq 1$, where the perpendicular wave number $k_\perp$ is estimated as $\sim 0.15 V_{Ae0}/\Omega_{e0}$.

The alternating variations in electron distribution due to cyclotron and Landau resonances also present in spatial space. Figure 5 shows the electron distribution f in the phase space (h, $v_\parallel$) at T_{t2} for $v_\perp/V_{Ae0} = 2$–4. A series of discrete cavity structures with decreased f labeled as #1-#7 are observed around the cyclotron resonance velocity v_c, while the island structures with increased f labeled as #I-#VII are formed around Landau resonance velocity v_L. Alternating cavity and island structures appear in spatial space. They propagate in the same direction as chorus waves with the wave's group velocity (not shown), though the resonance velocities at which the island and cavity are formed are opposite in direction. Note that the spatial scale of each structure is $\sim 8 V_{Ae0}/\Omega_{e0}$, corresponding to
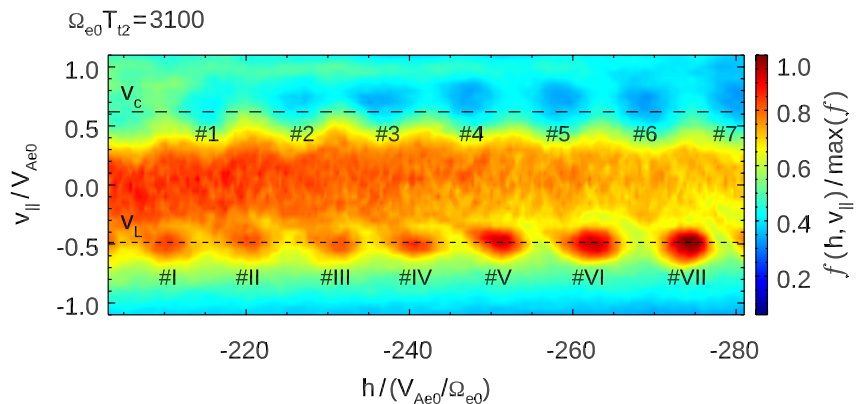

Figure 5. The distribution $f(h, v_\parallel)$ at $\Omega_{e0} T_{t2} = 3,100$, normalized to the maximum value in the plot. The dashed and dotted lines denote v_c and v_L, respectively. Seven cavity (island) structures around v_c (v_L) are labeled as #1-#7 (#I-#VII).

the wavelength of chorus waves ($2\pi/k = 7.95V_{Ae0}/\Omega_{e0}$). It indicates that the density fluctuation in oblique chorus waves is due to the wave-particle interactions through both cyclotron and Landau resonances.

4. Discussion

Electron holes are commonly detected in the wave phase of rising tone chorus waves (H. Chen, Lu, et al., 2022; Nunn, 1974; Omura et al., 2008; Tao et al., 2021). In this study, we have found that the central position of electron hole in ζ oscillates under of subpackets. The total number densities within the electron hole are evaluated to be comparable at subpacket peaks and troughs in the simulation, indicating that the number of trapped electrons remains nearly unchanged during subpacket formation. However, the locations of trapped electrons in ζ are varied, leading to different energy transfer during electron hole oscillation. At subpacket peaks, electron hole mainly locates in $\zeta \approx -\pi - \pi/2$ corresponding to an inhomogeneity factor of $S \sim -0.4$, implying the maximum energy transfer between electrons and chorus waves. The particles' energy gain is calculated by $\Delta W = -\int_0^\infty \int_0^{2\pi} \int_{-\infty}^\infty f(u_\parallel, \zeta, u_\perp) ev \cdot \delta E u_\perp du_\parallel d\zeta du_\perp$. We have found $\Delta W < 0$ at subpacket peaks, while $\Delta W \gtrsim 0$ at subpacket troughs. The amplitude modulation during subpacket formation at a fixed position is controlled by two terms: the energy transfer term ΔW between waves and particles, and the convection term $v_g \partial(\delta B)/\partial h$. The term ΔW is associated with the absolute nonlinear growth rate, determining the amplitude variation along wave packet $d(\delta B)/dt$ (Omura, 2021). The amplitude variation of subpacket at a specific position is given by $\partial(\delta B)/\partial t = d(\delta B)/dt - v_g \partial(\delta B)/\partial h$. From subpacket peaks to troughs, the convection term dominates, resulting in a decrease in wave amplitude $\partial(\delta B)/\partial t < 0$. On the other hand, from subpacket troughs to peaks, the energy transfer term dominates, leading to an increase in wave amplitude $\partial(\delta B)/\partial t > 0$.

The inhomogeneity factor S holds significant importance in nonlinear theory (Omura et al., 2008; Tao et al., 2021; Vomvoridis et al., 1982; Zonca et al., 2022). Theoretical study was first proposed by Omura et al. (2008) that S is fixed at ~-0.4 in chorus element excitation. However, we have found that S could change during subpacket formation. The values of S estimated from electron hole in our simulation is well verified by the S_{th} given by Equation 2, indicating that the irregular frequency chirping between adjacent subpackets (Crabtree, Gurudas Ganguli, & Tejero, 2017; H. Chen, Wang, et al., 2023; Santolík et al., 2014; Tsurutani et al., 2020; Zhang et al., 2020) is due to nonlinear physics. By assuming $S \sim -0.4$, Vomvoridis et al. (1982) proposed the well-known relationship between the chirping rate of chorus element and wave amplitude. This relationship is only valid for subpacket peaks, implying that the chorus element spectrum can be considered as composed of sub-packet peaks.

The variations in electron distributions have been proposed to significantly influence the frequency chirping and nonlinear growth of chorus waves (Trakhtengerts, 1995; Zonca et al., 2022). In this study, we have found that these variations exhibit as "plateau" and "bump" shapes in the parallel direction, and hole and hill structures in the perpendicular direction. In addition, the nongyrotropic distributions in the stationary gyrophase are also observed. All these variations of electron distribution could contribute to the nonlinear physics in the evolution of oblique chorus waves.

5. Conclusions

Various electron distributions associated with the formation of oblique chorus wave subpackets are investigated by performing a 2-D GCPIC simulation in a dipole field. These distributions are embedded with significant information of nonlinear physics involved in wave-particle interactions. Our primary conclusions are as follows:

1. Cyclotron and Landau resonances alternately take effects in the nonlinear wave-particle interaction during subpacket formation. They can generate alternating "bump" and "plateau" patterns in the momentum space, as well as the cavity and island structures in the spatial space.
2. Electron holes due to cyclotron resonance are observed in the wave phase space, and oscillate in size with time during subpacket formation. The inhomogeneity factor S associated with the electron holes does not remain constant as previously assumed; instead, S is ~-0.4 at subpacket peaks, while S is ~0 at subpacket troughs. At subpacket peaks, the energy transfer between waves and particles reaches the maximum. These results suggest a modified theory taking into account the variation of S is required for explaining subpacket formation.
3. Nongyrotropic electron distributions presenting in both wave gyrophase and stationary gyrophase are detected in the simulation.

Data Availability Statement

The data used to produce figures in this manuscript are available in Wang et al. (2023).

References

An, X., Li, J., Bortnik, J., Decyk, V., Kletzing, C., & Hospodarsky, G. (2019). Unified view of nonlinear wave structures associated with whistler-mode chorus. *Physical Review Letters*, *122*(4), 045101. https://doi.org/10.1103/PhysRevLett.122.045101

Burtis, W. J., & Helliwell, R. A. (1969). Banded chorus a new type of VLF radiation observed in the magnetosphere by OGO 1 and OGO 3. *Journal of Geophysical Research*, *74*(11), 3002–3010. https://doi.org/10.1029/ja074i011p03002

Chen, H., Chen, R., Gao, X., Lu, Q., Ke, Y., & Kong, Z. (2023). Unraveling the role of electron plateau distributions in the power gap formation of chorus waves: Van Allen Probes observations. *Geophysical Research Letters*, *50*(6), e2023GL102748. https://doi.org/10.1029/2023GL102748

Chen, H., Gao, X., Lu, Q., Fan, K., Ke, Y., Wang, X., & Wang, S. (2022). Gap formation around 0.5Ωe in the whistler mode waves due to the plateau-like shape in the parallel electron distribution: 2D PIC simulations. *Journal of Geophysical Research: Space Physics*, *127*(5), e2021JA030119. https://doi.org/10.1029/2021JA030119

Chen, H., Lu, Q., Wang, X., Fan, K., Chen, R., & Gao, X. (2022). One-dimensional gcPIC-δf simulation of hooked chorus waves in the Earth's inner magnetosphere. *Geophysical Research Letters*, *49*(4), e2022GL097989. https://doi.org/10.1029/2022GL097989

Chen, H., Wang, X., Chen, L., Omura, Y., Tsurutani, B., Lin, Y., & Xia, Z. (2023). Evolution of chorus subpackets in the Earth's magnetosphere. *Geophysical Research Letters*, *50*(21), e2023GL105938. https://doi.org/10.1029/2023GL105938

Chen, L., Breneman, A. W., Xia, Z., & Zhang, X.-J. (2020). Modeling of bouncing electron microbursts induced by ducted chorus waves. *Geophysical Research Letters*, *47*(17), e2020GL089400. https://doi.org/10.1029/2020GL089400

Chen, L., Thorne, R. M., Li, W., & Bortnik, J. (2013). Modeling the wave normal distribution of chorus waves. *Journal of Geophysical Research: Space Physics*, *118*(3), 1074–1088. https://doi.org/10.1029/2012JA018343

Chen, R., Tsurutani, B. T., Gao, X., Lu, Q., Chen, H., Lakhina, G. S., & Hajra, R. (2022). The structure and microstructure of rising-tone chorus with frequencies crossing at f ∼0.5 fce. *Journal of Geophysical Research: Space Physics*, *127*(8), e2022JA030438. https://doi.org/10.1029/2022JA030438

Coroniti, F. V., Scarf, F. L., Kennel, C. F., Kurth, W. S., & Gurnett, D. A. (1980). Detection of Jovian whistler mode chorus: Implications for the Io torus aurora. *Geophysical Research Letters*, *7*(1), 45–48. https://doi.org/10.1029/gl007i001p00045

Crabtree, C., Ganguli, G., & Tejero, M. (2017). Analytical and numerical analysis of self-consistent whistler wave Hamiltonian. *Plasma Physics and Controlled Fusion*, *59*(11), 114002. https://doi.org/10.1088/1361-6587/aa837a

Crabtree, C., Gurudas Ganguli, G., & Tejero, E. (2017). Analysis of self-consistent nonlinear wave-particle interactions of whistler waves in laboratory and space plasmas. *Physics of Plasmas*, *24*(5), 056501. https://doi.org/10.1063/1.4977539

Denton, R. E., Menietti, J. D., Goldstein, J., Young, S. L., & Anderson, R. R. (2004). Electron density in the magnetosphere. *Journal of Geophysical Research*, *109*(A9), A09215. https://doi.org/10.1029/2003JA010245

Foster, J. C., Erickson, P. J., & Omura, Y. (2021). Subpacket structure in strong VLF chorus rising tones: Characteristics and consequences for relativistic electron acceleration. *Earth Planets and Space*, *73*(1), 140. https://doi.org/10.1186/s40623-021-01467-4

Hanzelka, M., Santolík, O., Omura, Y., Kolmašová, I., & Kletzing, C. A. (2020). A model of the subpacket structure of rising tone chorus emissions. *Journal of Geophysical Research: Space Physics*, *125*(8), e2020JA028094. https://doi.org/10.1029/2020JA028094

Harada, Y., Andersson, L., Fowler, C. M., Mitchell, D. L., Halekas, J. S., Mazelle, C., et al. (2016). MAVEN observations of electron-induced whistler mode waves in the Martian magnetosphere. *Journal of Geophysical Research: Space Physics*, *121*(10), 9717–9731. https://doi.org/10.1002/2016JA023194

Horne, R. B., & Thorne, R. M. (1998). Potential waves for relativistic electron scattering and stochastic acceleration during magnetic storms. *Geophysical Research Letters*, *25*(15), 3011–3014. https://doi.org/10.1029/98GL01002

Hospodarsky, G. B., Averkamp, T. F., Kurth, W. S., Gurnett, D. A., Menietti, J. D., Santolik, O., & Dougherty, M. K. (2008). Observations of chorus at Saturn using the Cassini radio and plasma wave science instrument. *Journal of Geophysical Research*, *113*(A12), A12206. https://doi.org/10.1029/2008ja013237

Hsieh, Y.-K., & Omura, Y. (2023). Precipitation rates of electrons interacting with lower-band chorus emissions in the inner magnetosphere. *Journal of Geophysical Research: Space Physics*, *128*(6), e2023JA031307. https://doi.org/10.1029/2023JA031307

Kubota, Y., & Omura, Y. (2018). Nonlinear dynamics of radiation belt electrons interacting with chorus emissions localized in longitude. *Journal of Geophysical Research: Space Physics*, *123*(6), 4835–4857. https://doi.org/10.1029/2017JA025050

Liu, S., Xiao, F., Yang, C., He, Y., Zhou, Q., Kletzing, C. A., et al. (2015). Van Allen Probes observations linking radiation belt electrons to chorus waves during 2014 multiple storms. *Journal of Geophysical Research: Space Physics*, *120*(2), 938–948. https://doi.org/10.1002/2014JA020781

Lu, Q., Ke, Y., Wang, X., Liu, K., Gao, X., Chen, L., & Wang, S. (2019). Two-dimensional general curvilinear particle-in-cell (gcPIC) simulation of rising-tone chorus waves in a dipole magnetic field. *Journal of Geophysical Research: Space Physics*, *124*(6), 4157–4167. https://doi.org/10.1029/2019JA026586

Meredith, N. P., Horne, R. B., & Anderson, R. R. (2001). Substorm dependence of chorus amplitudes: Implications for the acceleration of electrons to relativistic energies. *Journal of Geophysical Research*, *106*(A7), 13165–13178. https://doi.org/10.1029/2000JA900156

Miyoshi, Y., Oyama, S., Saito, S., Kurita, S., Fujiwara, H., Kataoka, R., et al. (2015). Energetic electron precipitation associated with pulsating aurora: EISCAT and Van Allen Probes observations. *Journal of Geophysical Research: Space Physics*, *120*(4), 2754–2766. https://doi.org/10.1029/2014JA020690

Nunn, D. (1974). A self-consistent theory of triggered VLF emissions. *Planetary and Space Science*, *22*(3), 349–378. https://doi.org/10.1016/0032-0633(74)90070-1

Nunn, D., Zhang, X.-J., Mourenas, D., & Artemyev, A. V. (2021). Generation of realistic short chorus wave packets. *Geophysical Research Letters*, *48*(7), e2020GL092178. https://doi.org/10.1029/2020GL092178

Omura, Y. (2021). Nonlinear wave growth theory of whistler-mode chorus and hiss emissions in the magnetosphere. *Earth Planets and Space*, *73*(1), 1–28. https://doi.org/10.1186/s40623-021-01380-w

Omura, Y., Hsieh, Y.-K., Foster, J. C., Erickson, P. J., Kletzing, C. A., & Baker, D. N. (2019). Cyclotron acceleration of relativistic electrons through Landau resonance with obliquely propagating whistler-mode chorus emissions. *Journal of Geophysical Research: Space Physics*, *124*(4), 2795–2810. https://doi.org/10.1029/2018JA026374

Omura, Y., Katoh, Y., & Summers, D. (2008). Theory and simulation of the generation of whistler-mode chorus. *Journal of Geophysical Research*, *113*(A4), A04223. https://doi.org/10.1029/2007JA012622

Omura, Y., & Nunn, D. (2011). Triggering process of whistler mode chorus emissions in the magnetosphere. *Journal of Geophysical Research*, *116*(A5), A05205. https://doi.org/10.1029/2010JA016280

O'Neil, T. (1965). Collisionless damping of nonlinear plasma oscillations. *Physics of Fluids*, *8*(12), 2255–2262. https://doi.org/10.1063/1.1761193

Ozaki, M., Shiokawa, K., Miyoshi, Y., Hosokawa, K., Oyama, S., Yagitani, S., et al. (2018). Microscopic observations of pulsating aurora associated with chorus element structures: Coordinated Arase satellite-PWING observations. *Geophysical Research Letters*, *45*(22), 12125–12134. https://doi.org/10.1029/2018GL079812

Santolík, O., Gurnett, D. A., Pickett, J. S., Parrot, M., & Cornilleau-Wehrlin, N. (2003). Spatio-temporal structure of storm-time chorus. *Journal of Geophysical Research*, *108*(A7), 1278. https://doi.org/10.1029/2002JA009791

Santolík, O., Kletzing, C. A., Kurth, W. S., Hospodarsky, G. B., & Bounds, S. R. (2014). Fine structure of large-amplitude chorus wave packets. *Geophysical Research Letters*, *41*(2), 293–299. https://doi.org/10.1002/2013GL058889

Tao, X., Zonca, F., & Chen, L. (2017). Identify the nonlinear wave-particle interaction regime in rising tone chorus generation. *Geophysical Research Letters*, *44*(8), 3441–3446. https://doi.org/10.1002/2017GL072624

Tao, X., Zonca, F., & Chen, L. (2021). A "trap-release-amplify" model of chorus waves. *Journal of Geophysical Research: Space Physics*, *126*(9), e2021JA029585. https://doi.org/10.1029/2021JA029585

Thorne, R. M., Li, W., Ni, B., Ma, Q., Bortnik, J., Chen, L., et al. (2013). Rapid local acceleration of relativistic radiation-belt electrons by magnetospheric chorus. *Nature*, *504*(7480), 411–414. https://doi.org/10.1038/nature12889

Trakhtengerts, V. Y. (1995). Magnetosphere cyclotron maser: Backward wave oscillator generation regime. *Journal of Geophysical Research*, *100*(A9), 17205–17210. https://doi.org/10.1029/95JA00843

Tsurutani, B. T., Chen, R., Gao, X., Lu, Q., Pickett, J. S., Lakhina, G. S., et al. (2020). Lower-band "monochromatic" chorus riser subelement/wave packet observations. *Journal of Geophysical Research: Space Physics*, *125*(10), e2020JA028090. https://doi.org/10.1029/2020JA028090

Tsurutani, B. T., & Smith, E. J. (1974). Postmidnight chorus: A substorm phenomenon. *Journal of Geophysical Research*, *79*(1), 118–127. https://doi.org/10.1029/JA079i001p00118

Vomvoridis, J. L., Crystal, T. L., & Denavit, J. (1982). Theory and computer simulations of magnetospheric very low frequency emissions. *Journal of Geophysical Research*, *87*(A3), 1473–1489. https://doi.org/10.1029/JA087iA03p01473

Wang, X., Chen, H., Omura, Y., Hsieh, Y., Chen, L., Lin, Y., et al. (2023). Database of "resonant electron signatures in the formation of chorus wave subpackets" [Dataset]. *Zenodo*. https://doi.org/10.5281/zenodo.10403672

Xiao, F., Su, Z., Zheng, H., & Wang, S. (2009). Modeling of outer radiation belt electrons by multidimensional diffusion process. *Journal of Geophysical Research*, *114*(A3), A03201. https://doi.org/10.1029/2008JA013580

Xiao, F., Su, Z., Zheng, H., & Wang, S. (2010). Three-dimensional simulations of outer radiation belt electron dynamics including cross-diffusion terms. *Journal of Geophysical Research*, *115*(A5), A05216. https://doi.org/10.1029/2009JA014541

Zhang, X.-J., Mourenas, D., Artemyev, A. V., Angelopoulos, V., Kurth, W. S., Kletzing, C. A., & Hospodarsky, G. B. (2020). Rapid frequency variations within intense chorus wave packets. *Geophysical Research Letters*, *47*(15), e2020GL088853. https://doi.org/10.1029/2020GL088853

Zonca, F., Tao, X., & Chen, L. (2022). A theoretical framework of chorus wave excitation. *Journal of Geophysical Research: Space Physics*, *127*(2), e2021JA029760. https://doi.org/10.1029/2021JA029760